



## Projected refractive index framework for multi-wavelength phase retrieval

YUNHUI GAO AND LIANGCAI CAO\*

State Key Laboratory of Precision Measurement Technology and Instruments, Department of Precision Instruments, Tsinghua University, Beijing 100084, China

\*Corresponding author: clc@tsinghua.edu.cn

Received 27 September 2022; revised 26 October 2022; accepted 26 October 2022; posted 27 October 2022; published 10 November 2022

**Multi-wavelength phase retrieval provides a competitive solution to lensless holographic imaging that features a low-cost, compact design and high data acquisition speed. However, the existence of phase wraps poses a unique challenge for iterative reconstruction, and the resulting algorithms often suffer from limited generalizability and increased computational complexity. Here, we propose a projected refractive index framework for multi-wavelength phase retrieval that directly recovers the amplitude and unwrapped phase of the object. General assumptions are linearized and integrated into the forward model. Based on an inverse problem formulation, physical constraints and sparsity priors are incorporated, which ensures imaging quality under noisy measurements. We experimentally demonstrate high-quality quantitative phase imaging on a lensless on-chip holographic imaging system using three color LEDs.**

© 2022 Optica Publishing Group

<https://doi.org/10.1364/OL.476707>

Phase retrieval underlies many optical imaging techniques where direct access to the phase information is not possible. It takes an alternative approach to physically encode the phase information into the intensity variations that can be recorded by imaging sensors. Such an encoding scheme, also known as diversity measurement, can be achieved in various ways, such as using multiple imaging distances, wavefront modulations, sample translations, illumination angles, or illumination wavelengths. Among the existing diversity measurement schemes, wavelength diversity has gained considerable research interest in recent years due to its unique advantages over other existing methods [1–9]. First, compared with other encoding mechanisms, the size of the entire imaging system can be reduced significantly. Such compactness allows portable applications in resource-limited areas and *in situ* monitoring of biological dynamics inside an incubator [10–12]. Second, by using low-cost color LEDs as the light source, it provides a cost-effective solution for microscopic imaging applications [13,14]. Third, the data acquisition speed can be much higher because the measurement procedure does not involve any mechanical displacements. The temporal resolution can be even further improved using a color sensor and wavelength multiplexing [15–20].

Despite its unique potential, multi-wavelength phase retrieval poses challenges in terms of numerical reconstruction, which should be addressed with particular care. Conventional multi-wavelength phase retrieval algorithms are typically some variants of the classical alternating projection algorithms [21], which iteratively recover the object complex transmission function. For imaging of optically thick samples, however, the existence of phase wraps is problematic for phase conversion during the reconstruction. To address this problem, conventional algorithms rely on phase unwrapping operations or dedicated processing steps [22]. This further increases the computational complexity and complicates the algorithmic behavior.

In this Letter, we propose an efficient algorithmic framework for multi-wavelength phase retrieval that directly recovers the projected refractive index of the object. It obviates the need for computationally costly phase unwrapping steps. Based on an inverse problem formulation, physical constraints and sparsity priors can be easily integrated, offering much flexibility to various applications.

Figure 1(a) shows a typical multi-wavelength in-line holographic imaging system. The object is illuminated sequentially by monochromatic waves with wavelengths  $\lambda_1, \lambda_2, \dots, \lambda_K$ . Meanwhile, the corresponding intensity images of the diffracted field are recorded by the imaging sensor. The relative phase shift  $\phi_i$  induced by the object with respect to the  $i$ th wavelength is given by  $\phi_i = 2\pi n_i l / \lambda_i$ , where  $n_i$  is the difference of the refractive index between the medium and the environment and  $l$  is the thickness of the object. Assuming the object absorption and refractive index are independent of the wavelength, we have

$$\alpha_1 = \alpha_2 = \dots = \alpha_K, \quad (1)$$

$$\lambda_1 \phi_1 = \lambda_2 \phi_2 = \dots = \lambda_K \phi_K, \quad (2)$$

where  $\alpha_i$  denotes the amplitude transmission at the  $i$ th wavelength. The above assumptions generally hold for transparent biological specimens or a relatively small wavelength tuning range. In conventional phase retrieval problems, the object transmission function  $\mathbf{x}_i = \alpha_i \exp(j\phi_i)$  is treated as the unknown variable. The vectorized forward model is given by

$$\mathbf{y}_i = |\mathbf{A}_i \mathbf{x}_i|, \quad i = 1, 2, \dots, K, \quad (3)$$

where  $\mathbf{x}_i \in \mathbb{C}^n$ ,  $\mathbf{A}_i \in \mathbb{C}^{m \times n}$ , and  $\mathbf{y}_i \in \mathbb{R}^m$  denote the object transmission function, sampling matrix, and modulus measurement

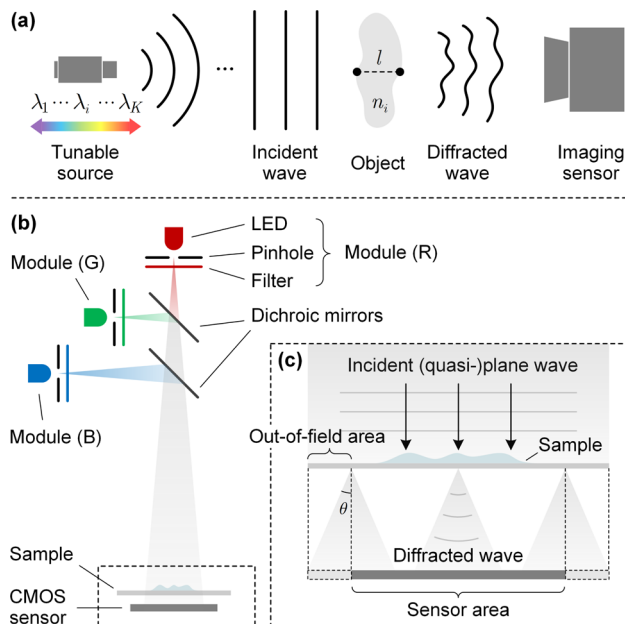


**Fig. 1.** (a) Schematic of a multi-wavelength in-line holographic imaging system. (b) Experimental setup using three color LEDs for illumination. (c) Diffraction model, where the diffraction angle  $\theta$  is determined by the sampling frequency.

with respect to the  $i$ th out of  $K$  wavelengths. The sampling matrix  $A_i$  is determined by the specific optical configuration of the imaging system and may consist of any linear transforms such as free-space propagation, mask modulation, etc. According to the basic assumptions of Eqs. (1) and (2), the object transmission functions  $x_1, x_2, \dots, x_K$  are related to each other via

$$|x_1| = |x_2| = \dots = |x_K|, \quad (4)$$

$$\lambda_1 U(\arg x_1) = \lambda_2 U(\arg x_2) = \dots = \lambda_K U(\arg x_K), \quad (5)$$

where  $U$  denotes the phase unwrapping operation. The main difficulty of solving the conventional multi-wavelength phase retrieval problem arises from the fact that both Eqs. (4) and (5) are *nonlinear* with respect to the object transmission function  $x_i$ . As a result, most of the existing algorithms are heuristic in nature, which makes their algorithmic behaviors difficult to track and limits their range of applications. Furthermore, the phase unwrapping step leads to significantly increased computation time and vulnerability to noise.

Unlike conventional phase retrieval methods, the refractive framework takes the projected refractive index  $u_i = \phi_i - j \ln(\alpha_i)$  as the unknown variable, which is related to the object transmission function  $x_i$  via  $x_i = \exp(ju_i)$  [23,24]. The forward model is then given by

$$y_i = |A_i \exp(ju_i)|, \quad i = 1, 2, \dots, K. \quad (6)$$

The amplitude and phase are given by  $\alpha_i = \exp[-\text{Im}(u_i)]$  and  $\phi_i = \text{Re}(u_i)$  for the  $i$ th wavelength, respectively. As is shown in Fig. 2(a), the phase is no longer limited within the range of  $[-\pi, \pi]$ , but can instead take any values on the real axis. According to Eqs. (1) and (2), the physical constraints are expressed as

$$\text{Im}(u_1) = \text{Im}(u_2) = \dots = \text{Im}(u_K), \quad (7)$$

$$\lambda_1 \text{Re}(u_1) = \lambda_2 \text{Re}(u_2) = \dots = \lambda_K \text{Re}(u_K). \quad (8)$$

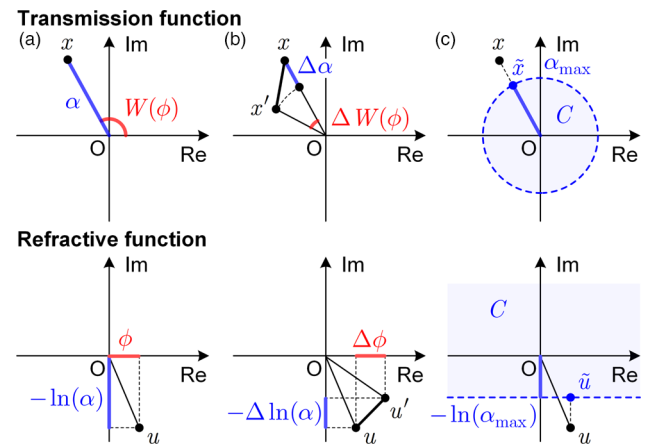


**Fig. 2.** Illustrative comparison between the transmission function  $x$  and the refractive function  $u$ . (a) Relations of the amplitude  $\alpha$  and phase  $\phi$ , where  $W$  denotes the phase wrapping operation. (b) Finite difference calculation, where  $x'$  and  $u'$  denote the transmission function and the refractive function of the adjacent pixel, respectively. (c) Enforcing the absorption constraint via projection, where  $\tilde{x}$  and  $\tilde{u}$  denote the projected transmission function and refractive function, respectively.

It is worth noticing that, unlike in the case of the conventional approach, the amplitude and phase constraints are now *linear* with respect to  $u_i$ . As a result, they can be directly integrated into the forward model of Eq. (6) as

$$y_i = \left| A_i \exp \left[ j \frac{\lambda_1}{\lambda_i} \text{Re}(u) - \text{Im}(u) \right] \right|, \quad i = 1, 2, \dots, K, \quad (9)$$

where the subscript is omitted because the only variable is  $u = u_1$ . The constrained problem of Eqs. (3)–(5) is transformed into a much easier one as given by Eq. (9) via a surprisingly simple change of variables.

Based on the forward model of Eq. (9), multi-wavelength phase retrieval is reformulated as a regularized inverse problem:

$$\min_{u \in C} \frac{1}{2K} \sum_{i=1}^K \left\| A_i \exp \left[ j \frac{\lambda_1}{\lambda_i} \text{Re}(u) - \text{Im}(u) \right] - y_i \right\|_2^2 + \tau \|Du\|_1, \quad (10)$$

where  $\tau > 0$  is a regularization parameter,  $D \in \mathbb{R}^{2n \times n}$  denotes the finite difference operator, and  $C$  denotes a physical constraint set. Considering the nonconvexity of multi-wavelength phase retrieval, sparsity regularization and physical constraints are introduced to incorporate prior knowledge of the object and thus push the solution towards the desired direction [25]. In particular, we apply a complex total variation (TV) function enforcing piece-wise smoothness of the object. It calculates the  $\ell_1$  norm of the differences between adjacent pixels of a complex-valued image. It should be noted that, although complex TV can be used to calculate both the transmission function  $x_i$  and the refractive function  $u_i$ , their physical meanings are very different. As is illustrated in Fig. 2(b), in the refractive framework, the phase and amplitude differences are decoupled into the real and imaginary parts and thus contribute independently to the complex TV function. Apart from sparsity priors, we adopt a widely used nonnegative absorption constraint which assumes that the object is passive:  $C \stackrel{\text{def}}{=} \{x \in \mathbb{C}^n : |x| \leq \alpha_{\max}\} \equiv \{u \in \mathbb{C}^n : \text{Im}(u) \geq -\ln(\alpha_{\max})\}$ , where we can often set  $\alpha_{\max} = 1$

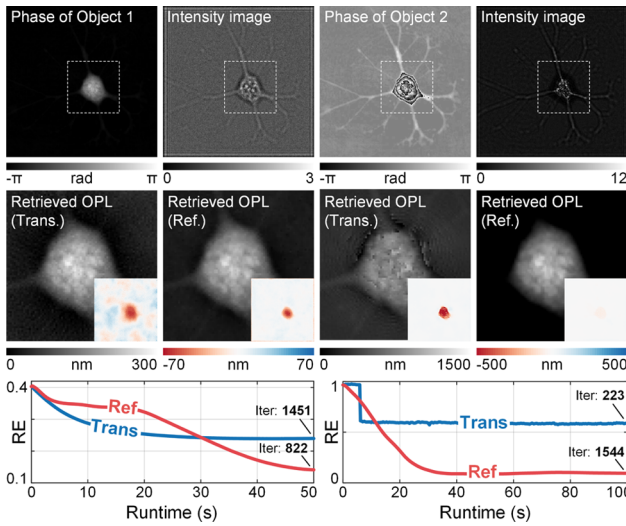


**Fig. 3.** Simulation results using two virtual objects with a maximum OPL of 300 nm (Object 1, two left-hand columns) and 1500 nm (Object 2, two right-hand columns). From top to bottom: the phase of the object and the intensity image corresponding to one wavelength; retrieved OPL (enlarged view); and the residual RE plotted against runtime.

if the intensity is properly normalized [26]. Figure 2(c) illustrates the absorption constraint set for the transmission function and the refractive function.

The problem of Eq. (10) is a nonsmooth composite optimization problem. Therefore, we adopt an accelerated variant of the proximal gradient method to solve this problem. Considering the nonconvexity of the problem, monotonicity is enforced during the iterations in order to guarantee a stable convergence. Readers are referred to [Supplement 1](#) for algorithm derivation and implementation details.

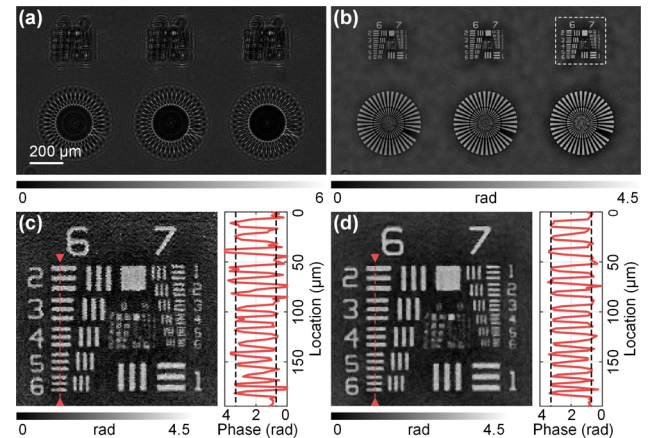
To evaluate the proposed algorithmic framework, we consider a lensless in-line holographic imaging system using three color LEDs for both simulated and optical experiments, as shown in Fig. 1(b). In this case, the sampling matrix  $A_i$  can be expressed explicitly as  $A_i = CQ_i$ , where  $C \in \mathbb{R}^{m \times n}$  denotes the image cropping operation to model the finite size of the sensor area. This is because the out-of-field object may also contribute to the diffraction intensity due to the linear convolution effect, as illustrated in Fig. 1(c).  $Q_i \in \mathbb{C}^{n \times n}$  denotes the free-space propagation with respect to the  $i$ th wavelength, which is calculated using the angular spectrum model. All numerical experiments were conducted using a personal computer with a Core i7-11700F CPU @ 2.50 GHz (Intel) and 16 GB of RAM.

Figure 3 shows a simulated comparison between the conventional phase retrieval algorithm based on the object transmission model and the proposed refractive framework. To facilitate a fair comparison, both algorithms are modified to accommodate the particular forward model of lensless on-chip microscopy, which is described in detail in [Supplement 1](#). A transparent virtual object of size  $256 \times 256$  is illuminated by three wavelengths (400, 500, and 600 nm) and the corresponding diffraction pattern for each wavelength is recorded 2 mm away by a sensor whose pixel size is  $5 \mu\text{m}$ . An additive white Gaussian noise with a signal-to-noise ratio of 20 dB is added to all intensity images. To facilitate a quantitative comparison, the relative error (RE) is calculated as  $\text{RE} = \|\mathbf{u} - \mathbf{u}^*\|_2 / \|\mathbf{u}^*\|_2$ , where  $\mathbf{u}$  and  $\mathbf{u}^*$  denote

the estimated and ground truth object refractive function, respectively. The algorithms are tested with two different objects. As shown by the two left-hand columns of Fig. 3, Object 1 has a maximum optical path length (OPL) of 300 nm, which is smaller than the illumination wavelengths. Therefore, conventional algorithms can be implemented without phase unwrapping. Both algorithms converge relatively fast, but the conventional one yields a larger reconstruction error due to its limited capability to cope with noise. In the second case, the maximum OPL induced by Object 2 is 1500 nm, which is much larger than all the illumination wavelengths. As a result, phase unwrapping is performed each iteration for the conventional algorithm, which significantly increases the computation complexity [27]. Furthermore, the phase conversion step is complicated by the fine details of the object. The algorithm tends to oscillate due to incorrect phase unwrapping at certain areas. In contrast, the proposed algorithm circumvents the phase wrapping problem and remains efficient as in the first case. The entire reconstruction process is provided in [Visualization 1](#).

We further validated the algorithm using experimentally collected data from a lensless in-line holographic imaging system. Three LEDs with center wavelengths of 625 nm (red), 530 nm (green), and 455 nm (blue) respectively were used as the light source. To ensure enough spatial and temporal coherence, a pin-hole (diameter  $500 \mu\text{m}$ ) and a bandpass filter (bandwidth  $\sim 10 \text{ nm}$ ) were placed in front of each LED [28]. The three beams were combined using two dichroic mirrors and then normally incident on the sample. The in-line holograms were recorded by a bare board CMOS sensor (Sony IMX226, pixel size  $1.85 \mu\text{m}$ , resolution  $4024 \times 3036$ ). The field of view is approximately the same as the sensor area, which is  $7.44 \text{ mm} \times 5.62 \text{ mm} \approx 41.81 \text{ mm}^2$ . The distance between the source and the sample was  $\sim 300 \text{ mm}$ . The sample-to-sensor distance was only  $\sim 2 \text{ mm}$ , the exact value of which can be determined using an autofocus algorithm. Under such a configuration, the incident wave can be approximated as a spatially and temporally coherent plane wave. The LEDs were lit up sequentially and in total three holograms were recorded for numerical reconstruction.

Figure 4 shows the imaging results of a quantitative phase microscopy target (Benchmark Technologies). The exposure



**Fig. 4.** Phase retrieval with noisy experimental data. (a) Intensity image and (b) retrieved phase corresponding to one wavelength. Enlarged results obtained by (c) the conventional algorithm and (d) the proposed algorithm. The cross-sectional profiles are plotted on the right, where the dashed lines indicate the theoretical phase value.

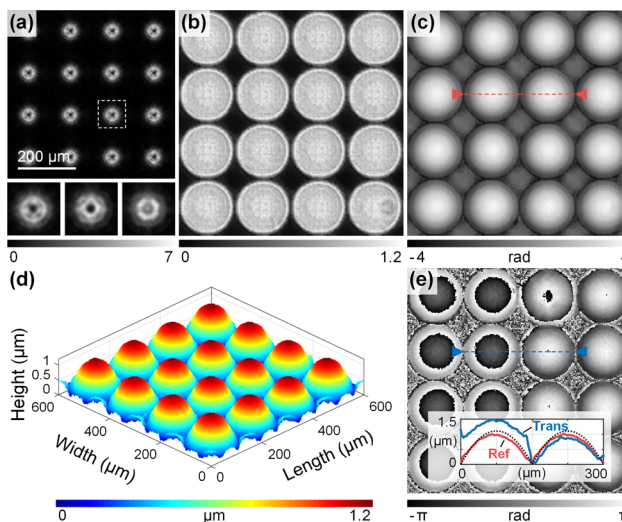


**Fig. 5.** Experimental characterization of a microlens array. (a)–(c) Intensity image, retrieved amplitude and phase corresponding to one wavelength by the proposed refractive framework. The inset of (a) shows the enlarged intensity image for all three wavelengths. (d) Calculated surface profiles of the sample. (e) Retrieved phase by the conventional algorithm. The inset shows the cross-sectional profiles, where the dashed line indicates the theoretical value.

time for each image was intentionally set to 0.2 ms, resulting in severely noisy observations. Noise robustness is essential for multi-wavelength phase retrieval based on LEDs, because the use of pinholes and spectral filters often leads to a significant loss of illumination power. The conventional algorithm and the proposed refractive framework were run for 50 iterations with a runtime of 24.89 s and 46.82 s, respectively. The retrieved phase by both algorithms generally agrees with the nominal value, but the proposed refractive framework yields better reconstruction quality with the help of the regularization techniques.

We further evaluated the algorithms using objects with wrapped phases. Figure 5 presents the imaging results of a microlens array (MLA150-5C-M, Thorlabs). The conventional algorithm has a much longer runtime (1231.25 s) due to the phase unwrapping step, whereas the proposed algorithm took only 103.36 s (both run for 100 iterations). Moreover, we observed that the conventional algorithm may be problematic when retrieving objects with small amplitude values. This is because the phase at these areas is not well confined and may thus take arbitrary values, leading to severe phase unwrapping errors, as shown in Fig. 5(e). In contrast, both large phase shifts and small amplitude values can be well addressed by the refractive method. The entire reconstruction process can be found at [Visualization 2](#).

To conclude, we have proposed a multi-wavelength phase retrieval algorithm based on the projected refractive index framework. It obviates the need of phase unwrapping steps during the reconstruction, thus improving the robustness and reducing the time consumption. Another promising feature of the refractive framework is that, by formulating multi-wavelength phase retrieval as a standard optimization problem, it offers great flexibility to accommodate various physical settings, noise

statistics, and also advanced image priors. On the theoretical side, since the refractive formulation is fundamentally different from the conventional one, issues regarding the uniqueness of the solutions and recovery guarantees also remain to be studied in the future. To facilitate future research, a MATLAB implementation of the algorithm is available in Ref. [29].

**Funding.** National Natural Science Foundation of China (61827825).

**Disclosures.** The authors declare no conflicts of interest.

**Data availability.** Data and code underlying the results presented in this paper are available in Ref. [29].

**Supplemental document.** See [Supplement 1](#) for supporting content.

## REFERENCES

- P. Bao, F. Zhang, G. Pedrini, and W. Osten, *Opt. Lett.* **33**, 309 (2008).
- Y. Liu, Q. Liu, Y. Li, B. Xu, J. Zhang, and Z. He, *Opt. Express* **29**, 7197 (2021).
- D. W. Noom, K. S. Eikema, and S. Witte, *Opt. Lett.* **39**, 193 (2014).
- Y. Bai, S. P. Vettil, X. Pan, C. Liu, and J. Zhu, *APL Photonics* **2**, 056101 (2017).
- L. Hervé, O. Cioni, P. Blandin, F. Navarro, M. Menneteau, T. Bordy, S. Morales, and C. Allier, *Biomed. Opt. Express* **9**, 5828 (2018).
- J. Mariën, R. Stahl, A. Lambrechts, C. van Hoof, and A. Yurt, *Opt. Express* **28**, 33002 (2020).
- G. I. Haham, O. Peleg, P. Sidorenko, and O. Cohen, *J. Opt.* **22**, 075608 (2020).
- C. Guo, F. Zhang, Y. Geng, X. Kan, J. Tan, S. Liu, and Z. Liu, *Optics and Lasers in Engineering* **137**, 106402 (2021).
- Q. Wang, J. Ma, and P. Su, *Front. Photon.* **3**, 865666 (2022).
- C. Allier, S. Morel, R. Vincent, L. Ghenim, F. Navarro, M. Menneteau, T. Bordy, L. Hervé, O. Cioni, X. Gidrol, Y. Usson, and J.-M. Dinten, *Cytometry* **91**, 433 (2017).
- O. Mandula, J.-P. Kleman, F. Lacroix, C. Allier, D. Fiole, L. Hervé, P. Blandin, D. C. Kraemer, and S. Morales, *Opt. Express* **28**, 2079 (2020).
- X. Wu, J. Sun, J. Zhang, L. Lu, R. Chen, Q. Chen, and C. Zuo, *Opt. Lett.* **46**, 2023 (2021).
- M. Sanz, J. Á. Picazo-Bueno, L. Granero, J. García, and V. Micó, *Sci. Rep.* **7**, 43291 (2017).
- Y. Fan, J. Li, L. Lu, J. Sun, Y. Hu, J. Zhang, Z. Li, Q. Shen, B. Wang, R. Zhang, Q. Chen, and C. Zuo, *Photonix* **2**, 19 (2021).
- M. Sanz, J. A. Picazo-Bueno, J. García, and V. Micó, *Opt. Express* **23**, 21352 (2015).
- O. Flasseur, C. Fournier, N. Verrier, L. Denis, F. Jolivet, A. Cazier, and T. Lépine, *Appl. Opt.* **56**, F189 (2017).
- Y. Zhou, J. Wu, Z. Bian, J. Suo, G. Zheng, and Q. Dai, *J. Biomed. Opt.* **22**, 066006 (2017).
- H. Zhang, T. Stangner, K. Wiklund, and M. Andersson, *Appl. Opt.* **57**, 9855 (2018).
- G. Zhou, S. Zhang, Y. Hu, and Q. Hao, *Opt. Express* **28**, 9976 (2020).
- W. Lee, D. Jung, S. Ryu, and C. Joo, *Opt. Express* **25**, 8398 (2017).
- J. R. Fienup, *Appl. Opt.* **21**, 2758 (1982).
- P. Bao, G. Pedrini, and W. Osten, *Opt. Commun.* **285**, 5029 (2012).
- F. Wittwer, J. Hagemann, D. Brückner, S. Flenner, and C. G. Schroer, *Optica* **9**, 295 (2022).
- S. Huhn, L. M. Lohse, J. Lucht, and T. Salditt, *Opt. Express* **30**, 32871 (2022).
- Y. Gao and L. Cao, “A complex constrained total variation image denoising algorithm with application to phase retrieval,” *arXiv*, arXiv:2109.05496 (2021).
- T. Latychevskaia and H.-W. Fink, *Phys. Rev. Lett.* **98**, 233901 (2007).
- J. M. Bioucas-Dias and G. Valadão, *IEEE Trans. on Image Process.* **16**, 698 (2007).
- J. Zhang, J. Sun, Q. Chen, and C. Zuo, *IEEE Transactions on Computational Imaging* **6**, 697 (2020).
- Y. Gao and L. Cao, “Projected refractive index framework for phase retrieval,” <https://github.com/THUHoloLab/refractive-phase-retrieval>.